

ACCELERATION OF X-RAY EMITTING ELECTRONS IN THE CRAB NEBULA

GWENAEL GIACINTI AND JOHN G. KIRK

Max-Planck-Institut für Kernphysik, Postfach 103980, 69029 Heidelberg, Germany

Draft version April 16, 2018

ABSTRACT

We study particle acceleration at the termination shock of a striped pulsar wind by integrating trajectories in a prescribed model of the magnetic field and flow pattern. Drift motion on the shock surface maintains either electrons or positrons on “Speiser” orbits in a ring-shaped region close to the equatorial plane of the pulsar, enabling them to be accelerated to very high energy by the first-order Fermi mechanism. A power-law spectrum results: $dN_e/d\gamma \propto \gamma^{\alpha_e}$, where α_e lies in the range -1.8 to -2.4 and depends on the downstream turbulence level. For sufficiently strong turbulence, $\alpha_e \simeq -2.2$, and both the photon index and the flux of 1–100 keV X-rays from the Crab Nebula, as measured by NuSTAR, can be reproduced. The particle spectrum hardens to $\alpha_e \simeq -1.8$ at lower turbulence levels, which may explain the hard photon index observed by the Chandra X-ray Observatory in the central regions of the Nebula.

Subject headings: acceleration of particles — plasmas — pulsars: general — shock waves — stars: winds, outflows — X-rays: individual (Crab)

1. INTRODUCTION

The photon index, $\Gamma = 2.1$, of the Crab Nebula in 1–100 keV X-rays (Madsen et al. 2015) is very close to that predicted for electrons accelerated by the first-order Fermi process at a relativistic shock front (Bednarz & Ostrowski 1998; Kirk et al. 2000; Achterberg et al. 2001). Is this just a coincidence? On the one hand, this mechanism is known to be inhibited at perpendicular shocks (Begelman & Kirk 1990; Sironi & Spitkovsky 2011; Summerlin & Baring 2012), such as that separating the pulsar wind from the Crab Nebula — the reason is that the magnetic field sweeps particles away from the shock in the downstream region, thereby preventing the multiple, stochastic shock crossings that characterize the Fermi process. On the other hand, the toroidal magnetic field transported through the shock into the Nebula is expected to change sign across the rotational equatorial plane of the pulsar (for reviews, see Amato 2014; Porth et al. 2017), giving rise to a broad current sheet, in which the Fermi process might still operate. To answer the question posed above, and determine the relevance of this process, we study particle acceleration in the equatorial sheet using a detailed model of the magnetic field there. We find that stochastic crossings and recrossings of the shock front are indeed responsible for acceleration, and that shock-induced drifts play a crucial role in focusing leptons of one sign of charge into the acceleration zone. Our main result is that both the photon index and the flux of X-rays can be reproduced by the combination of Fermi acceleration and drifts, if one assumes a turbulent amplitude $\delta B_a > 200 \mu\text{G}$ and an average toroidal field at higher latitudes of $B = 1 \text{ mG}$.

Recent, state-of-the-art, phenomenological modeling of the morphology of the Crab Nebula places significant constraints on the possible sites of particle acceleration. In particular, the X-ray to soft gamma-ray emission appears to originate from a torus-shaped region lying in the rotational equator of the Crab Pulsar, and located at a radius where the ram pressure of the pulsar wind roughly

equals that in the Nebula (Porth et al. 2014; Olmi et al. 2015). Furthermore, these models give insight into the global structure of the magnetic field, and the degree to which it is turbulent, making it possible to construct diffusion coefficients for energetic particles propagating in the outer Nebula (Porth et al. 2016). However, close to the relativistic termination shock (TS) that forms the inner edge of the Nebula, the energetic particle distribution is necessarily anisotropic (Kirk & Schneider 1987), so that diffusion coefficients cannot be used to model the transport process. Instead, we build a simplified, explicit model of the magnetic field and flow pattern in the equatorial region of the termination shock, based on the results of MHD simulations, and follow the trajectories of particles injected at the shock as they cross and recross it. Finally, we compute the radiation they emit after leaving the shock and cooling in the Nebula.

The magnetic field model, injection prescription and method of computing the radiation are described in §2, and the results found by analyzing particle trajectories in §3. A discussion of the application to the Crab Nebula is presented in §4.

2. DESCRIPTION OF THE MODEL

2.1. Regular magnetic field

Magnetohydrodynamic models of the Crab Nebula suggest that it is powered by a radially propagating pulsar wind, whose luminosity per unit solid angle is concentrated towards the rotational equator. The particle component, which we assume to be electrons and positrons, carries only a small fraction of the power close to launch, most of it being in the form of Poynting flux. However, the wind is thought to be striped (Coroniti 1990; Michel 1994), i.e., the magnetic field has a component that oscillates at the rotation frequency of the pulsar, as well as a phase-averaged or DC component. MHD models assume complete dissipation of the oscillating component before the plasma enters the Nebula downstream of the termination shock (Del Zanna et al. 2018). Whether this occurs somewhere in the wind, or at the shock itself, has

no influence on the downstream parameters, provided it proceeds without significant radiation losses (Lyubarsky 2003). The remaining, phase-independent magnetic field is carried into the Nebula, and reverses its sign across the rotational equator. Thus, an equatorial current sheet is formed, whose thickness depends on the latitude distribution of the oscillations, which, in turn, is determined by the inclination angle between the magnetic and rotation axes of the pulsar. The termination shock itself is oblate: in the equatorial region it is approximately spherical with radius roughly 4×10^{17} cm, but moves close in to the pulsar in the polar regions, where the power of the wind is low. Outside the current sheet, but still in the equatorial region, the ordered field is roughly 1 mG on the downstream side of the shock.

Here we adopt a planar model of the flow in the equatorial region, since the gyroradius of TeV–PeV electrons in a mG magnetic field is $\simeq 3 \times 10^{12-15}$ cm, much smaller than the radius of the shock. In cartesian coordinates, the shock is located in the $x = 0$ plane, and the equatorial plane is $z = 0$. In the downstream region, $x > 0$, the plasma is assumed to flow everywhere along $+\hat{\mathbf{x}}$ at $c/3$, as expected behind a strong, weakly magnetized, relativistic shock, and the current sheet is located at $-z_0 < z < z_0$. The downstream magnetic field, $\mathbf{B}_d(z)$, measured in the rest frame of the downstream fluid (DRF), is linearly interpolated between the values on the northern and southern edges of the current sheet:

$$\mathbf{B}_d(z) = \begin{cases} -B_{d,0}\hat{\mathbf{y}} & \text{if } z > z_0 \\ -B_{d,0}(z/z_0)\hat{\mathbf{y}} & \text{if } |z| \leq z_0 \\ +B_{d,0}\hat{\mathbf{y}} & \text{if } z < -z_0 \end{cases} \quad (1)$$

To find the corresponding field in the upstream region, we assume that the termination shock is a thin structure in which all incoming oscillations at the pulsar rotation frequency are dissipated. Applying Faraday’s law, together with a time-average over the pulsar period, one finds that the electric and magnetic fields upstream, $\mathbf{E}'_u(z)$ and $\mathbf{B}'_u(z)$, as measured in the shock rest frame (the “SRF”), are:

$$\mathbf{E}'_u(z) = \frac{1}{2\sqrt{2}} \times \begin{cases} +B_{d,0}\hat{\mathbf{z}} & \text{if } z > z_0 \\ +B_{d,0}(z/z_0)\hat{\mathbf{z}} & \text{if } |z| \leq z_0 \\ -B_{d,0}\hat{\mathbf{z}} & \text{if } z < -z_0 \end{cases} \quad (2)$$

$$\mathbf{B}'_u(z) = \frac{1}{2\sqrt{2}\beta_s} \times \begin{cases} -B_{d,0}\hat{\mathbf{y}} & \text{if } z > z_0 \\ -B_{d,0}(z/z_0)\hat{\mathbf{y}} & \text{if } |z| \leq z_0 \\ +B_{d,0}\hat{\mathbf{y}} & \text{if } z < -z_0 \end{cases} \quad (3)$$

where $\beta_s\hat{\mathbf{x}}$ is the 3-velocity of the upstream plasma in the SRF. Thus, for highly relativistic inflow, $\beta_s \approx 1$, the fields seen in the shock frame are, to a good approximation, equal to those of a vacuum electromagnetic wave. It follows that the particle trajectories are insensitive to the Lorentz factor $\Gamma_s = 1/\sqrt{1-\beta_s^2}$ of the upstream plasma. The oscillating component is not constrained by this analysis, but this is not important in the present context, since the gyroradius of particles injected into the acceleration process in the equatorial zone substantially exceeds the wavelength of the oscillations, which, therefore, provide only a small perturbation of the orbit computed in the phase-averaged field.

In the absence of turbulence, particles far from the equator undergo systematic drifts in either the positive

or negative \mathbf{x} -direction, superimposed upon the plasma bulk motion. Provided the drift motion in the plasma rest frame is slower than the plasma speed in the SRF, which is always true in the cases we consider, all particles move in the direction of the flow, i.e., towards the shock in the upstream, and away from it in the downstream region. However, a crucial, novel aspect is introduced by the reversal of the average field. Speiser orbits (Speiser 1965), which cross the plane $z = 0$, do not drift, but can propagate at arbitrary speed (consistent with their energy) in the $\pm\mathbf{x}$ directions. Thus, there exists a population of particles that is effectively disconnected from the local plasma speed, which facilitates repeated shock crossings. As a rough guide, a particle of energy $E_{\text{inj},d}$ injected into the field defined in Eq. (1) at height z above the equatorial plane follows a Speiser orbit if $|z| < z_{\text{crit}}$, where

$$z_{\text{crit}} = \sqrt{\frac{z_0 E_{\text{inj},d}}{e B_{d,0}}} \simeq 5.8 \times 10^{14} \text{ cm} \sqrt{\frac{z_{0,17} E_{\text{inj},d,12}}{B_{d,0,-3}}}, \quad (4)$$

where $z_{0,17} = z_0/(10^{17} \text{ cm})$, $B_{d,0,-3} = B_{d,0}/(1 \text{ mG})$, and $E_{\text{inj},d,12} = E_{\text{inj},d}/(1 \text{ TeV})$.

2.2. Turbulent magnetic field

Onto the large-scale magnetic field $\mathbf{B}_d(z)$, we superimpose a three-dimensional, homogeneous turbulent field, $\delta\mathbf{B}_d(x, y, z)$ (also defined in the DRF). This field satisfies $\langle \delta\mathbf{B}_d \rangle = \mathbf{0}$, where $\langle \dots \rangle$ denotes a spatial average, and its root-mean-square strength, $\delta B_d \equiv (\langle \delta\mathbf{B}_d^2 \rangle)^{1/2} > 0$, is independent of position. This implies that the level of turbulence, defined as $\delta B_d/B_d$ with $B_d = |\mathbf{B}_d|$, is larger at small $|z|$, in line with results from MHD simulations of pulsar wind nebulae, see for instance the upper right panel in Fig. 4 of Porth et al. (2016) where the largest levels of turbulence in the TS downstream are obtained around the equatorial plane.

We generate $\delta\mathbf{B}_d$ on 3D grids with $\mathcal{N} = 256$ vertices per side (256^3 grid points in total), following the method presented and tested in Giacinti et al. (2012). The grids repeat periodically in space, and the three cartesian components of $\delta\mathbf{B}_d$ are calculated at any point in space using an 8-point linear interpolation of their values on the 8 nearest vertices of the grid. We generate isotropic Bohm turbulence with power-spectrum $\mathcal{P}(k) \propto k^{-1}$, for wave vectors in the range $2\pi/L_{\text{max}} \leq k \leq 2\pi/L_{\text{min}}$, where L_{max} is the lateral size of the grid and L_{min} is twice the spacing between grid points. The dynamical range of the turbulence is, therefore, $L_{\text{max}}/L_{\text{min}} = \mathcal{N}/2 = 128$. We choose the spacing between grid points to be slightly smaller than half of the gyroradius in the strongest magnetic field in the injection zone of an electron with energy $E_{\text{inj},d}$ in the DRF. Taking smaller values does not noticeably affect the results. The value of L_{max} determines the high-energy cutoff in our simulated electron spectra, because particles with gyroradii larger than L_{max} experience little scattering and, therefore, no longer gain energy via the first-order Fermi mechanism. We have also tested other power-spectra, e.g., Kolmogorov ($\mathcal{P}(k) \propto k^{-5/3}$), and found no significant difference.

The Fermi process depends on the competing effects of advection and diffusion due to turbulence. Therefore, since particles injected at $|z| < z_{\text{crit}}$ follow trajectories resembling Speiser orbits, whereas those injected at

$|z| > z_{\text{crit}}$ are predominantly advected with the plasma, differences can be expected according to whether the level of turbulence at z_{crit} is smaller or larger than unity. We denote the dimensionless parameter characterizing these different acceleration regimes by

$$\eta_{\text{crit}} \equiv \delta B_d / B_d(z_{\text{crit}}), \quad (5)$$

and investigate a range of values covering small and large η_{crit} , whilst keeping the magnetic field at $z \sim z_0$ predominantly toroidal, as indicated by simulations (Porth et al. 2016).

The idealized, plane-parallel case with only a phase-averaged field in the upstream region introduces an unphysical feature into the particle kinematics: it permits particles moving very close to the equator to propagate unhindered to an arbitrarily large distance upstream of the shock. In reality, both the spherical geometry and irregularities in the oscillating and the phase-averaged fields prevent this behavior. In our simulations, we take account of this by adding to the upstream, phase-averaged component a small turbulent field that is purely magnetic as seen in the upstream rest frame (URF), in analogy with that added to the downstream field, but physically disconnected from it. This turbulent component maintains the conservation of particle energy measured in the URF, making it convenient to integrate the trajectories in this reference frame. To ensure that particles moving almost along $-\hat{x}$ experience resonant scattering we also stretch the grid in the upstream by a factor Γ_s along x . We have performed tests to ensure that the properties of this turbulent upstream field do not affect our results.

2.3. Injection

In an isotropic wind, the energy carried per particle in units of $m_e c^2$, after dissipation of the entire Poynting flux, is

$$\mu = \frac{L_{\text{s.d.}}}{\dot{N}_{\pm} m_e c^2}, \quad (6)$$

where $L_{\text{s.d.}}$ is the spin-down power of the neutron star, and \dot{N}_{\pm} the rate at which the particles are transported into the nebula by the wind. In the absence of a phase-averaged field, i.e., precisely on the equator, the results of Amano & Kirk (2013), Giacchè & Kirk (2017), and Kirk & Giacinti (2017), indicate that particles are effectively thermalized in a thin structure, termed an “electromagnetically modified shock front”. The majority of them are transmitted through this structure into the downstream region with energy in the DRF $E_{\text{inj,d}} = \gamma_{\text{inj,d}} m_e c^2 \approx \mu m_e c^2$, and a small fraction is reflected into the upstream region. To date, no computations of the shock structure with a non-vanishing phase-averaged field are available. Therefore, since the energy density in this field is small compared to the total energy density at all points in the equatorial zone we simulate, we assume particles are injected into the downstream plasma with the same value of $E_{\text{inj,d}}$ at all values of z , and with momentum directed along the shock normal. On the one hand, this overestimates the injection energy at finite $|z|$, but, on the other, it underestimates it by neglecting the reflected particles, and further underestimates the initial return probability by assuming

the angular distribution of the injected particles to be a collimated beam. The average value of μ over the entire lifetime of the Crab Nebula and over all directions of the wind is constrained to be $10^4 \lesssim \mu \lesssim 10^6$ (Olm et al. 2016; Porth et al. 2017); in our simulations, we choose $E_{\text{inj,d}} = 1 \text{ TeV}$, corresponding to $\gamma_{\text{inj,d}} \approx 2 \times 10^6$.

2.4. Simulated trajectories

We integrate the particle trajectories in the test-particle limit, by solving the Lorentz force equation in the upstream and downstream rest frames where the electric fields vanish. Each time a particle crosses the shock a Lorentz transformation of the momentum components is performed from the old rest frame to the new rest frame. Although it does not affect the final result, this procedure requires a specific choice of upstream Lorentz factor, for which we choose $\Gamma_s = 100$. In the DRF (URF), the shock is located at $x_d = -ct_d/3$ ($x_u = -\beta_s ct_u$). We note that advection of particles with the fluid flow is automatically taken into account by this procedure. We place an escape boundary in the downstream at $x = +d$, as measured in the SRF, and terminate each trajectory when it reaches $x = d$. We have verified that the results do not depend on d , provided it is larger than the gyroradius of the highest energy electrons present in the system. On the upstream side, particles cannot escape to $x \rightarrow -\infty$, because the shock always overtakes them. At each shock crossing all relevant physical quantities of the accelerated particles (energies in the DRF and SRF, momenta coordinates, positions, times) are stored. These are used, for example, to calculate the steady-state spectra of the accelerated electrons and positrons at the shock front.

2.5. Synchrotron emission from the nebula

The particles accelerated at the TS are ultimately advected into the nebula where they cool and emit synchrotron radiation. In a magnetic field B , the synchrotron power emitted per unit frequency interval by a single electron with pitch angle α and nonrelativistic (angular) gyrofrequency $\omega_g = eB/m_e c$ is

$$\frac{dL_{1p}^{\text{synch}}}{d\nu} = \sqrt{3} \alpha_f \hbar \omega_g \sin \alpha F(\nu/\nu_c), \quad (7)$$

where α_f is the fine-structure constant, $\nu_c = 3\gamma^2 \omega_g \sin \alpha / (4\pi)$ is the characteristic frequency, and the synchrotron function is

$$F(x) = x \int_x^\infty dt K_{5/3}(t), \quad (8)$$

where $K_{5/3}$ is a modified Bessel function. In the following, we neglect the dependence on pitch angle by setting $\sin \alpha = \sqrt{2/3}$ and approximate the synchrotron function by $F(x) = 1.85 x^{1/3} \exp(-x)$ (cf. Melrose 1980). The resulting total luminosity per unit frequency interval is

$$J(\nu) = \int d\gamma N_c(\gamma) \frac{dL_{1p}^{\text{synch}}}{d\nu}, \quad (9)$$

where $N_c(\gamma) = dN_c/d\gamma$ is the differential number of cooled electrons in the interval $d\gamma$ in the nebula, and we have implicitly assumed a homogeneous magnetic field within the radiation zone. For a source at a distance D from Earth, the differential energy flux is $F_\nu =$

$J(\nu)/(4\pi D^2)$. Synchrotron losses imply $\dot{\gamma} = -\beta\gamma^2$ with $\beta = \sigma_{\text{T}}B^2/(6\pi m_e c)$ and σ_{T} the Thomson cross section, and one finds, in the steady state regime,

$$N_c(\gamma) = \frac{1}{\beta\gamma^2} \int_{\gamma}^{\infty} d\gamma' Q(\gamma'), \quad (10)$$

where $Q(\gamma)d\gamma$ is the number of particles accelerated at the TS and “injected” into the nebula per time unit with a Lorentz factor between γ and $\gamma + d\gamma$.

We set

$$Q(\gamma_d) = \begin{cases} Q_0 \gamma_d^{\alpha_e} & \text{for } f E_{\text{inj,d}}/m_e c^2 \leq \gamma_d \leq E_{\text{max}}/m_e c^2 \\ 0 & \text{otherwise} \end{cases} \quad (11)$$

and determine the spectral index, α_e , from the results described in § 3.2. The parameter f is chosen such that the simulated particle spectrum at the TS is a power-law at $E_d \geq f \times E_{\text{inj,d}}$. Typically, we find $f = 3$ to 7. Particles of energy less than $f \times E_{\text{inj,d}}$ are neglected in (11), but they influence only the low frequency synchrotron spectrum, $\nu \lesssim (f E_{\text{inj,d}}/m_e c^2)^2 \omega_g$. We do not attempt to model the spectrum of the Nebula in this energy range, since it is less well-known, because of the uncertainty associated with the contribution of the pulsar, and the difficulties involved in modelling absorption (Kirsch et al. 2005). The limited dynamical range of the turbulence in our simulation introduces an artificial upper limit to the power law distribution of accelerated particles. In reality, however, this quantity, E_{max} , is determined by radiative losses, even though these can be neglected over most of the acceleration range. Setting the loss-time, $\tau_{\text{sync}} = 6\pi m_e^2 c^3 / (\sigma_{\text{T}} B^2 E)$, equal to the time to complete one half of a gyration, $\tau_{1/2} = \pi E / (e B c)$, at $E = E_{\text{max}}$, leads to

$$E_{\text{max}} = \sqrt{\frac{6m_e^2 c^4 e}{\sigma_{\text{T}} B}} \simeq 1.1 \text{ PeV } B_{-3}^{-1/2}, \quad (12)$$

where $B_{-3} = B/(1 \text{ mG})$.

As we will see in Section 3, particles are accelerated to high energies only if they are injected in a region of the TS close to the equatorial plane. Therefore, to avoid computing uninteresting trajectories, we introduce a free parameter \mathcal{F}_{inj} , which we vary between roughly 5% and 20%, according to the particular simulation, and select for the injection region the range $|z| \leq \mathcal{F}_{\text{inj}} z_0$. The normalization factor Q_0 depends on the fraction, $\epsilon_{\text{acc,f}}$, of particles injected at $|z| \leq \mathcal{F}_{\text{inj}} z_0$ that are accelerated to $E_d \geq f \times E_{\text{inj,d}}$. We determine $\epsilon_{\text{acc,f}}$ numerically.

Let us assume that the equatorial region of the TS is approximately spherical with a radius r_{TS} , and that the region at $|z| \leq \mathcal{F}_{\text{inj}} z_0$ in our planar 1D simulations corresponds to a ring-shaped region of the TS whose half-width, as viewed from the pulsar, subtends an angle $\Theta_{1/2} = \mathcal{F}_{\text{inj}} z_0 / r_{\text{TS}}$. In this geometry, the angle Θ between the rotation and magnetic axes of the pulsar satisfies $\Theta = z_0 / r_{\text{TS}}$. The angular dependence of the wind power, $dL_{\text{s.d.}}/d\Omega$, can be modeled as being proportional to $\sin^n \vartheta$, where ϑ is the colatitude, and the index n lies between 2 (when the magnetic and rotation axes are aligned) and 4 (when they are orthogonal) (Tchekhovskoy et al. 2016). The angular dependence of the particle component, however, is not well constrained.

Here, we assume it has the same functional form, so that the rate at which electrons (or positrons) are injected at $|z| \leq \mathcal{F}_{\text{inj}} z_0$ is

$$\dot{N}_{\pm,\text{inj}} \approx (dL_{\text{s.d.}}/d\Omega)_{\vartheta=\pi/2} \sin \Theta_{1/2} / E_{\text{inj,d}} \quad (13)$$

and Q_0 of Eq. (11) is

$$Q_0 = \frac{(\alpha_e + 1) \epsilon_{\text{acc,f}} \dot{N}_{\pm,\text{inj}}}{(\gamma_{\text{max}}^{\alpha_e+1} - \gamma_{\text{min}}^{\alpha_e+1})} \times \begin{cases} 1 & \text{for } n = 0 \\ 1.5 & \text{for } n = 2 \\ 1.9 & \text{for } n = 4 \end{cases} \quad (14)$$

where $\gamma_{\text{min}} = f E_{\text{inj,d}}/m_e c^2$ and $\gamma_{\text{max}} = E_{\text{max}}/m_e c^2$.

3. RESULTS

3.1. Trajectories of electrons and positrons

First, we examine particle trajectories in the region of the TS that is close to the equatorial plane, in the sense that $|z| \lesssim z_{\text{crit}}$. (We show below that this region is the most favorable for electron acceleration.) In the upper row of Fig. 1, several trajectories in the SRF are plotted for electrons (upper left panel) and positrons (upper right panel) injected at the TS at $|z|/z_0 \leq 0.015$, with $z_0 = 10^{17} \text{ cm}$. All other parameters are set to the values discussed in § 2. In particular, the injection energy is $E_{\text{inj,d}} = 1 \text{ TeV}$, the magnetic field at z_0 is 1 mG ($B_{\text{d},0,-3} = 1$), and the pulsar polarity is such that $B_{\text{d},0} > 0$. In the following, we refer to “electrons” and “positrons” for this pulsar polarity. For the opposite polarity, the situation for electrons and positrons is inverted. The four solid lines (magenta, red, green, and blue) in both panels represent typical particle trajectories, calculated for $\delta B_d = 30 \mu\text{G}$, and projected onto the (x, z) plane. The level of turbulence, $\delta B_d/B_d = 3/(z/10^{15} \text{ cm})$, at $z = z_{\text{crit}}$ is, therefore, $\eta_{\text{crit}} \sim 5$. We show only examples of particles which return to the shock and enter the upstream region. In the simulations, most injected particles ($\sim 90\%$) escape downstream without experiencing acceleration. The upstream region is on the left hand side of the panels, at $x < 0$, and the downstream is on the right hand side, at $x > 0$. The shock position is denoted by a thin vertical black line at $x = 0$, and the equatorial plane is marked by a dotted black line at $z = 0$. By comparing the two upper panels of Fig. 1, one can clearly see that electrons and positrons behave differently. The drift-like motion imposed on crossing and recrossing the shock pushes positrons away from the equatorial plane, i.e. their $|z|$ tends to increase with time, whereas electrons are pushed towards $z = 0$ and remain on orbits close to, or around, the equatorial plane. Despite the perturbations introduced by the turbulent field, several of these electrons spend time on trajectories that closely resemble Speiser orbits, e.g., the magenta trajectory at $x < 0$, in the upper left panel. The fact that shock-drift systematically focuses the electrons into the equatorial plane has a positive impact on their acceleration: electrons tend to re-enter the downstream in regions with larger turbulence levels $\delta B_d/B_d$, and thence have a non-negligible probability to be scattered back into the upstream and continue to gain energy via the first-order Fermi mechanism. Indeed, one can see that the electrons plotted in the upper left panel cross and re-cross the TS several times. The lower left panel shows the trajectory of another electron accelerated to high energy. One can see that this electron spends most of

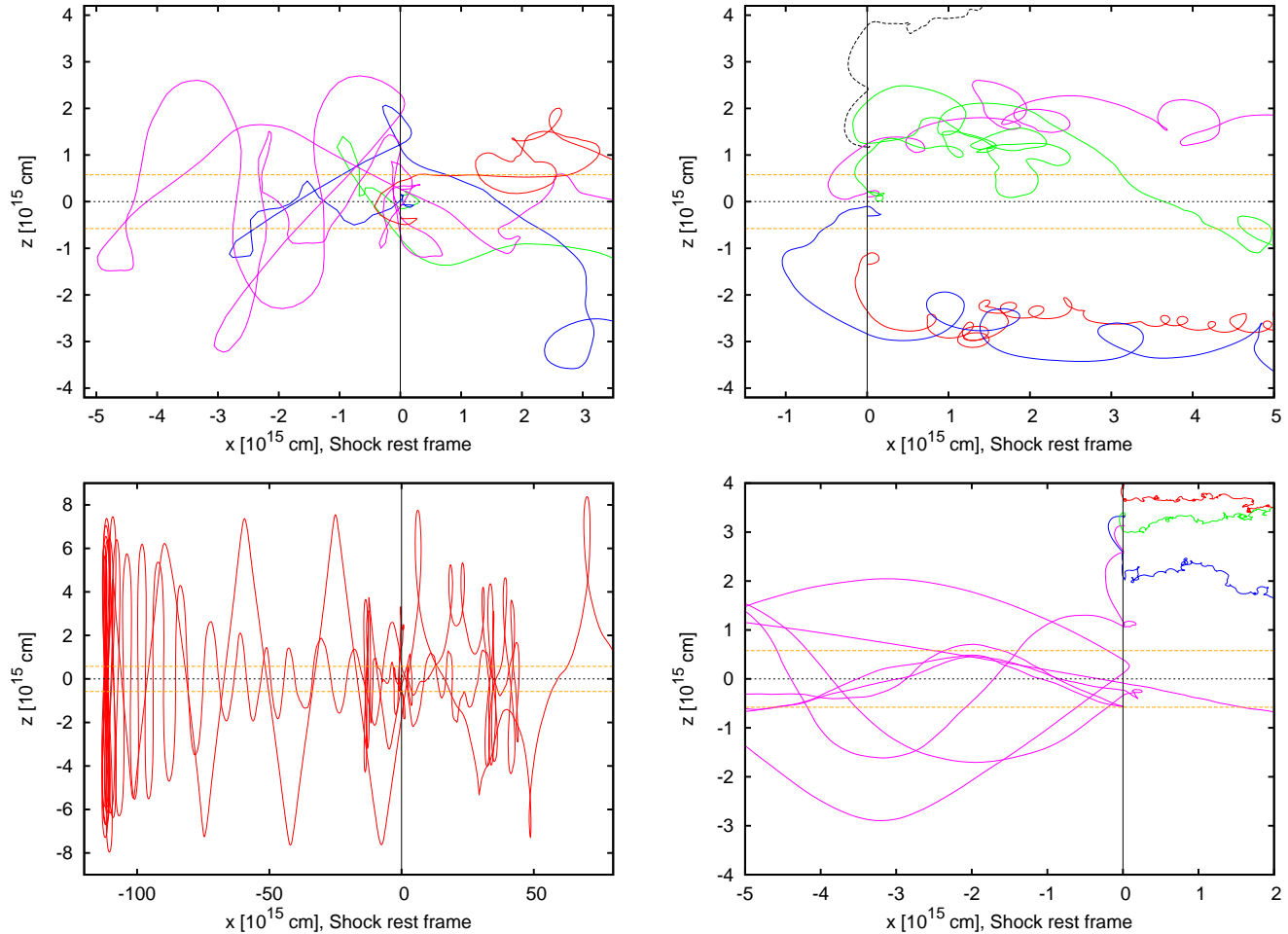


FIG. 1.— Upper row and lower left panel: trajectories of electrons (left panels) and positrons (upper right panel) injected at $|z|/z_0 \leq 0.015$, for $\delta B_d = 30 \mu\text{G}$ (solid curves in the three panels) or $\delta B_d = 400 \mu\text{G}$ (black dashed curve in the upper right panel). Lower right panel: trajectories of electrons injected at $|z|/z_0 > 0.015$, and for $\delta B_d = 400 \mu\text{G}$. In all four panels, trajectories are plotted in the SRF and projected onto (x, z) . The parameters are $z_0 = 10^{17}$ cm, $B_{d,0} = 1$ mG, and $E_{\text{inj},d} = 1$ TeV. The vertical black solid lines at $x = 0$ denote the shock position, the horizontal black dotted lines the equatorial plane ($z = 0$), and the orange dashed lines the critical distance $\pm z_{\text{crit}}$ from the equatorial plane.

its time on Speiser orbits, although it spends some time on a drift orbit, cf. the two loops in the downstream at $x \approx (1.5 - 2.5) \times 10^{16}$ cm and $z \approx (3 - 5) \times 10^{15}$ cm. The orbits appear irregular because of particle scattering induced by the turbulent magnetic fields. We confirm that accelerated electrons remain focused around the equatorial plane by plotting in Fig. 2 the distribution of the normalized shock crossing altitudes z/z_0 of electrons injected at $|z|/z_0 \leq 0.015$. In total, 5×10^6 particles are injected. We again use $\delta B_d = 30 \mu\text{G}$ in this example, and verified that results are not significantly different for $\delta B_d = 400 \mu\text{G}$. Three energy bands are shown, see the key in the figure. One can clearly see that the electrons cross and re-cross the TS in a small region around $z = 0$, with a typical width of a few percent of z_0 . Even though the size of this region increases with electron energy E_s (measured in the SRF), this is only due to the increase of the particle gyroradius. We checked that electrons always remain well confined and focused around $z = 0$, even at the highest energies.

In contrast, the situation for positrons is less favorable. As can be seen in the upper right panel of Fig. 1, those that cross the TS and enter the upstream at $z = z_1$ re-

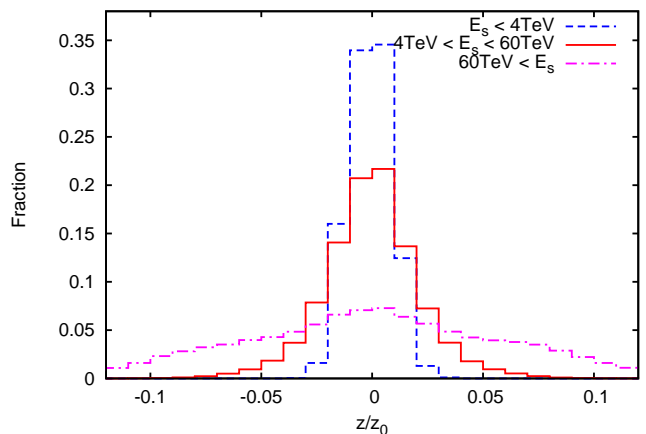


FIG. 2.— Distributions of normalized shock crossing altitudes, z/z_0 , for electrons with energies $E_s < 4$ TeV (dashed blue line), $4 \text{ TeV} < E_s < 60$ TeV (solid red line) and $E_s > 60$ TeV (magenta dash-dotted line) at the time of shock crossing. Electrons are injected at $|z|/z_0 \leq 0.015$. $\delta B_d = 30 \mu\text{G}$, and the other parameters are set to the same values as in Fig. 1.

enter the downstream at $|z| > |z_1|$. This is clearly visible for the red and blue trajectories at $z < 0$. This forces the positrons to re-enter the downstream in regions where turbulence levels are lower. They are then more likely to be advected away from the shock due to the stronger toroidal field at larger $|z|$, and this shuts down the first-order Fermi mechanism. Out of the four plotted positron trajectories, three of them complete only one cycle (i.e., downstream \rightarrow upstream \rightarrow downstream), and only one performs two (green trajectory). Increasing the strength of the turbulence in the downstream increases the probability for positrons to complete more cycles: The dashed black line shows a positron trajectory for $\delta B_d = 400 \mu\text{G}$, which completes two cycles. However, even in this case, acceleration quickly stops once the shock-induced drift pushes the particle to larger $|z|$ where the turbulence levels are smaller. One can see that this particle is advected in the downstream at $z \simeq 4 \times 10^{15}$ cm. Acceleration again stops more quickly than for electrons. The orange dashed lines in Fig. 1 show the altitudes where $z = \pm z_{\text{crit}}$. For these parameter values, $z_{\text{crit}} \simeq 0.0058 z_0$. It is interesting to note that in the downstream, the ∇B -drift is strongest around $|z| \approx (1 - 3) \times z_{\text{crit}}$, and is directed towards the shock for positrons, both at $z > 0$ and $z < 0$. In other words, the ∇B -drift helps the positrons injected in these regions to fight against advection, and it increases their chances to enter into the upstream for their first cycle (e.g., the first half-gyration in the downstream for the red and blue trajectories in the upper right panel in Fig. 1). Ultimately, however, this is to no avail, because of the effect of shock-drift during the first cycle.

In the lower right panel of Fig. 1, we show the trajectories of four electrons injected further from the equatorial plane, at $3 \times 10^{15} \text{ cm} < z < 4 \times 10^{15} \text{ cm}$, and take $\delta B_d = 400 \mu\text{G}$, the other parameter values remaining unchanged. It is apparent that shock-drift pushes all these electrons closer to $z = 0$. Because of the lower turbulence levels in the downstream at these larger $|z|$, the probability for a particle in the downstream to be scattered back into the upstream is smaller, and out of the four plotted trajectories, only one of them reaches the equatorial plane (the magenta line). The other three are advected away downstream after only one or a very few cycles. For example, the green trajectory completes one excursion into the upstream, whereas the blue one completes three. These electrons do gain some energy, thanks to the first-order Fermi effect and the shock-induced drift. However, the electron with the magenta trajectory gains significantly more energy than the others, because it reaches the equatorial plane region, which is the most favorable one for particle acceleration. Once an electron enters this region, it remains on Speiser orbits, as do those injected at $|z|/z_0 < 0.015$ — see the oscillations between $z > 0$ and $z < 0$ in the upstream.

3.2. Particle spectrum close to the equatorial plane

We calculate now the energy spectrum of the particles injected and accelerated in the equatorial region of the TS. The injection region where particles are most likely to reach high energies is typically within a few z_{crit} from the equatorial plane. We denote the height of this region by z_w , and find (cf. Sect. 3.3) $z_w \approx 5 \times 10^{14}$ cm for $z_0 = 10^{16}$ cm, $z_w \approx 1.5 \times 10^{15}$ cm for $z_0 = 10^{17}$ cm, and $z_w \approx 3.6 \times 10^{15}$ cm for $z_0 = 6 \times 10^{17}$ cm. In the follow-

ing, we consider the latter two cases. For each tested set of parameters, we inject 5×10^6 particles at points equally spaced in z in this region and construct the spectrum by recording the particle energy in the DRF at each shock crossing. Since particles do not change their energy whilst in the DRF, the steady state spectrum at the shock, averaged over all injection points, is identical to the spectrum of particles at $x = d$, where they are considered to have escaped. However, much better statistics are achieved by binning the spectrum at each shock crossing, rather than only at escape. We plot the steady state spectrum in the DRF, without taking into account the particles that have been advected in the downstream without being accelerated, i.e., the spectra shown hereafter refer to particles that have performed at least one cycle.

In Fig. 3 (left panel), we plot the spectra $E_d \times dN/dE_d$ of electrons (thick solid lines) and positrons (dashed lines) injected at $|z|/z_0 \leq 0.015$ for $z_0 = 10^{17}$ cm (i.e. $|z|/z_{\text{crit}} \leq 2.6$), and for two levels of turbulence in the downstream: $\delta B_d = 30 \mu\text{G}$ (red lines) and $\delta B_d = 400 \mu\text{G}$ (blue lines), corresponding to a level of turbulence at $z = z_{\text{crit}}$ of $\eta_{\text{crit}} = 5.2$ and $\eta_{\text{crit}} = 69$, respectively. The positron spectra are much softer than the electron spectra, even in the most favorable case of strong turbulence in the downstream, $\delta B_d = 400 \mu\text{G}$. This confirms the trend found in the previous subsection: only electrons are efficiently accelerated, whereas positrons are expelled from the acceleration region before they can reach high energies. The electron spectra in Fig. 3 extend to $E_d \sim (100 - 300) \text{ TeV}$. These high-energy cutoffs are an artifact. They occur at the energy at which the electron gyroradius equals the maximum size L_{max} of the grid on which the turbulent field is defined, above which the scattering is strongly suppressed. Below this cutoff and above $E_d \gtrsim 4 \text{ TeV}$, i.e., above a few times the injection energy, the spectra are well described by power-laws. To guide the eye, we plot two power-laws: one $\propto E_d^{-1.2}$ (thin dashed black line), and the other $\propto E_d^{-0.8}$ (thin dotted black line). One can clearly see that the electron spectral index depends on δB_d , being $\alpha_e \simeq -1.8$ for $\delta B_d = 30 \mu\text{G}$, and $\alpha_e \simeq -2.2$ for $\delta B_d = 400 \mu\text{G}$. We note that the latter value of α_e is compatible with the index expected for particles accelerated at a relativistic shock with pure scattering and no large-scale magnetic field (Achterberg et al. 2001). In Fig. 3 (right panel), we plot electron spectra for a wider range of values of δB_d : $\delta B_d = 0.3 \mu\text{G}$ (solid grey line), $0.6 \mu\text{G}$ (dashed blue), $1 \mu\text{G}$ (solid green), $60 \mu\text{G}$ (solid red), and $200 \mu\text{G}$ (dashed magenta), corresponding to levels of turbulence at z_{crit} of $\eta_{\text{crit}} = 0.052, 0.10, 0.17, 10, \text{ and } 35$. The electron spectrum is seen to be slightly softer than $E_d^{-2.2}$ for $\delta B_d = (0.3 - 1) \mu\text{G}$. It hardens to $dN/dE_d \propto E_d^{-1.8}$ for $\delta B_d = 60 \mu\text{G}$, and softens again for larger turbulence levels — the dotted magenta line for $\delta B_d = 200 \mu\text{G}$ is compatible with an index $-2.2 < \alpha_e < -1.8$. All curves are normalized to the same (arbitrary) level, which shows that, for low levels of turbulence $\delta B_b < 1 \mu\text{G}$, a smaller fraction of the injected electrons are accelerated.

In Table 1, seventh column, we give the fraction, $\epsilon_{\text{acc},3}$, of injected electrons that are accelerated to $E_d \geq 3 \text{ TeV}$. For $\delta B_b < 1 \mu\text{G}$, $\epsilon_{\text{acc},3}$ quickly drops, but otherwise remains in the range $\simeq 4 - 8\%$. In the fourth column of

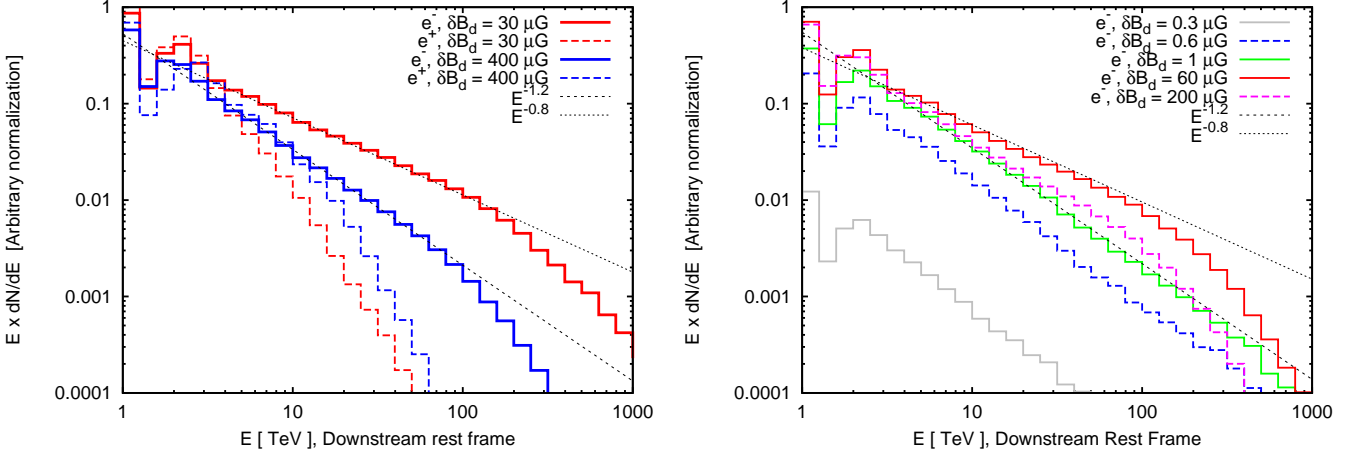


FIG. 3.— Left panel: spectra $E_d \times dN/dE_d$ of electrons (thick solid lines) and positrons (dashed lines) in the DRF, for $\delta B_d = 30 \mu\text{G}$ (red lines, corresponds to $\eta_{\text{crit}} = 5.2$) and $\delta B_d = 400 \mu\text{G}$ (blue lines, $\eta_{\text{crit}} = 69$); Right panel: Spectra $E_d \times dN/dE_d$ of electrons for $\delta B_d = 0.3, 0.6, 1, 60, 200 \mu\text{G}$ (i.e. $\eta_{\text{crit}} = 0.052, 0.10, 0.17, 10, 35$). See the key for the corresponding line types and colors. In both panels, $z_0 = 10^{17} \text{cm}$, $B_{d,0} = 1 \text{mG}$, and the particles are injected at $|z|/z_{\text{crit}} \leq 2.6$ (i.e. $|z|/z_0 \leq 0.015$) with $E_{\text{inj},d} = 1 \text{TeV}$. For reference, the thin black dashed (resp. dotted) lines show power-laws $\propto E_d^{-1.2}$ (resp. $\propto E_d^{-0.8}$).

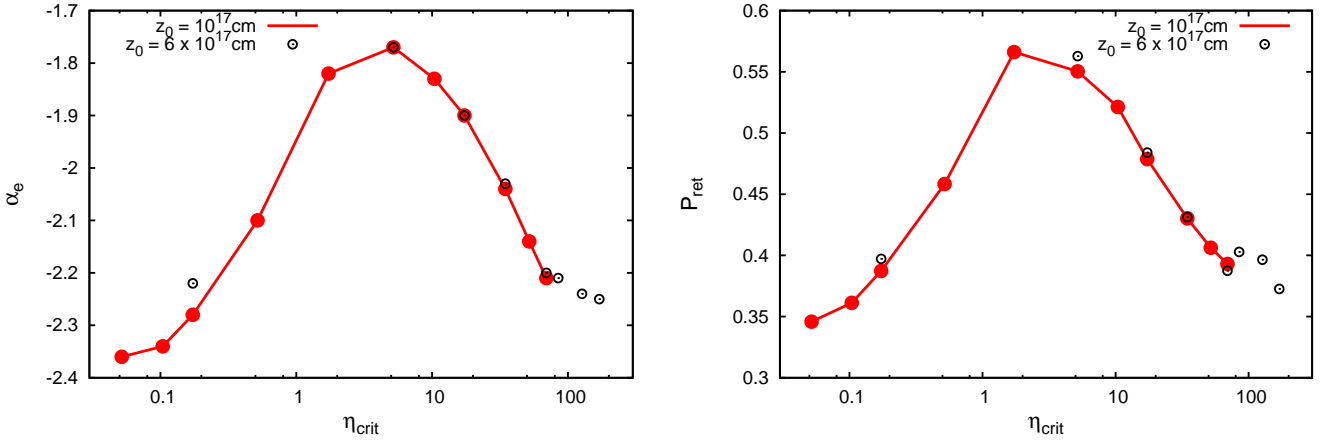


FIG. 4.— Left panel: Electron spectral index α_e as a function of η_{crit} (Fits on the interval $7 \text{TeV} \leq E_d \leq 80 \text{TeV}$). Right panel: Return probability \mathcal{P}_{ret} as a function of η_{crit} , for electrons with $7 \text{TeV} \leq E_d \leq 80 \text{TeV}$. On both panels, solid red lines are for $z_0 = 10^{17} \text{cm}$, and open black circles for $z_0 = 6 \times 10^{17} \text{cm}$. $B_{d,0} = 1 \text{mG}$, and the electrons are injected at $|z|/z_{\text{crit}} \leq 2.6$ (i.e. $|z|/z_0 \leq 0.015/\sqrt{z_0/10^{17} \text{cm}}$) with $E_{\text{inj},d} = 1 \text{TeV}$.

Table 1, we provide the values of α_e for $z_0 = 10^{17} \text{cm}$ and δB_d within the range $(0.3 - 400) \mu\text{G}$, and for $z_0 = 6 \times 10^{17} \text{cm}$ and $\delta B_d = (0.41 - 400) \mu\text{G}$. The third column contains the corresponding values of η_{crit} . The spectral indexes are calculated by fitting the electron spectra on the energy interval $7 \text{TeV} \leq E_d \leq 80 \text{TeV}$ where they are well described by power-laws.

In Fig. 4 (left panel), we plot α_e versus η_{crit} . The red line and filled red dots are for $z_0 = 10^{17} \text{cm}$, and the open black circles are for $z_0 = 6 \times 10^{17} \text{cm}$. The shape of the red curve confirms the trend already noted in Fig. 3. The spectrum is soft, with $\alpha_e \simeq -(2.3 - 2.2)$, at small ($\lesssim 1$) and large ($\gtrsim 30$) values of η_{crit} , i.e. small and large values of δB_d . It hardens at intermediate values of η_{crit} , and the index reaches its maximum of $\alpha_e \simeq -1.8$ around $\eta_{\text{crit}} \simeq$ a few, i.e. when the turbulence level at z_{crit} is close to unity. The results for α_e versus η_{crit} are almost the same for both values of z_0 , which suggests that α_e is a function of η_{crit} . We note that, at $B_{d,0}$ fixed,

$$\eta_{\text{crit}} \propto \delta B_d \times \sqrt{z_0}.$$

In the nonrelativistic theory of diffusive shock acceleration, the spectral index α_e is determined by the ratio of the average return probability of electrons from downstream to upstream, \mathcal{P}_{ret} , and their average relative energy gain per cycle, $\Delta E/E$ (Bell 1978). The relativistic theory is more complicated, since the (angular dependent) ratio of these quantities must be convolved with the actual angular distribution of particles at the shock. Nevertheless, these quantities, separately averaged, give a good intuitive guide to the mechanisms at work. In the fifth and sixth columns of Table 1, we give the values of \mathcal{P}_{ret} and $(\Delta E/E)_d$, (i.e., $\Delta E/E$ as measured in the DRF) respectively, for electrons with energies $7 \text{TeV} \leq E_d \leq 80 \text{TeV}$. No clear trend emerges for $(\Delta E/E)_d$, and results are compatible with $(\Delta E/E)_d$ being almost constant and $\simeq 1.1$. On the other hand, \mathcal{P}_{ret} shows a strong variation with η_{crit} . In Fig. 4 (right panel), we plot \mathcal{P}_{ret} versus η_{crit} for $z_0 = 10^{17} \text{cm}$ and

TABLE 1
SIMULATIONS WITH INJECTION CLOSE TO THE EQUATORIAL PLANE

$z_0/(10^{17} \text{ cm})$	$\delta B_d/(1 \mu\text{G})$	Turbulence level η_{crit}	Electron index α_e	Return probability \mathcal{P}_{ret}	Gain per cycle $(\Delta E/E)_d$	Fraction at $> 3 \text{ TeV}$ $\epsilon_{\text{acc},3}$
1	0.3	5.2×10^{-2}	-2.36 ± 0.03	0.35	1.05	1.1×10^{-3}
1	0.6	0.10	-2.34 ± 0.02	0.36	1.07	2.1×10^{-2}
1	1	0.17	-2.28 ± 0.02	0.39	1.06	4.4×10^{-2}
1	3	0.52	-2.10 ± 0.02	0.46	1.08	6.9×10^{-2}
1	10	1.7	-1.82 ± 0.03	0.57	1.07	8.4×10^{-2}
1	30	5.2	-1.77 ± 0.01	0.55	1.10	5.7×10^{-2}
1	60	10	-1.83 ± 0.01	0.52	1.11	5.3×10^{-2}
1	100	17	-1.90 ± 0.01	0.48	1.09	5.2×10^{-2}
1	200	35	-2.04 ± 0.01	0.43	1.09	4.7×10^{-2}
1	300	52	-2.14 ± 0.02	0.41	1.09	4.8×10^{-2}
1	400	69	-2.21 ± 0.01	0.39	1.08	4.5×10^{-2}
6	0.41	0.17	-2.22 ± 0.01	0.40	1.05	3.2×10^{-2}
6	12	5.2	-1.77 ± 0.01	0.56	1.09	6.3×10^{-2}
6	41	17	-1.90 ± 0.01	0.48	1.11	5.0×10^{-2}
6	82	35	-2.03 ± 0.02	0.43	1.14	4.4×10^{-2}
6	163	69	-2.20 ± 0.03	0.39	1.13	4.7×10^{-2}
6	200	85	-2.21 ± 0.03	0.40	1.16	4.9×10^{-2}
6	300	1.3×10^2	-2.24 ± 0.04	0.40	1.14	4.6×10^{-2}
6	400	1.7×10^2	-2.25 ± 0.05	0.37	1.16	4.2×10^{-2}

NOTE. — Electrons are injected at $|z|/z_{\text{crit}} \leq 2.6$ corresponding to $|z|/z_0 \leq 0.015/\sqrt{z_0/(10^{17} \text{ cm})}$. The injection energy is $E_{\text{inj},d} = 1 \text{ TeV}$ and the regular magnetic field at z_0 is $B_{d,0} = 1 \text{ mG}$.

$z_0 = 6 \times 10^{17} \text{ cm}$, with the same color code as in the left panel. The good match between the open black circles and the red curve shows that \mathcal{P}_{ret} is also a function of η_{crit} . By comparing the left and the right panels in Fig. 4, one sees that α_e and \mathcal{P}_{ret} are strongly correlated. The return probability of electrons is maximal ($\mathcal{P}_{\text{ret}} \approx 0.6$) at values of η_{crit} where the electron spectrum is hardest, and it is smaller ($\mathcal{P}_{\text{ret}} \approx 0.35 - 0.4$) at values of η_{crit} where the electron spectrum is soft, $\alpha_e \approx -(2.3 - 2.2)$. This implies that the hard electron spectrum found at $\eta_{\text{crit}} \sim (1 - 10)$ is due to an increase in the return probability of the electrons from the downstream to the upstream at these turbulence levels. The reason is connected with the nature of the drift trajectories, combined with the fact that for $\eta \sim 1$, the role of turbulence is significant on those sections of the orbit closer to the equatorial plane (low altitude, i.e., smaller $|z|$), and relatively unimportant on those at higher altitude (larger $|z|$). Electron drift trajectories move away from the shock front ($\dot{x} > 0$) at low altitude, and towards it at high altitude. Since the turbulence scatters predominantly the low altitude section, the net result is reduction in \dot{x} , i.e., in the escape probability.

3.3. Overall electron spectrum at the termination shock

We now investigate the acceleration, or lack thereof, of electrons injected further away from the equatorial plane. In Fig. 5, we plot the spectra $E_d \times dN/dE_d$ of electrons injected at the TS in six different zones of equal area, located at successively increasing distance from the equatorial plane (see caption). The first column corresponds to $\delta B_d = 30 \mu\text{G}$, the second to $\delta B_d = 100 \mu\text{G}$, and the third to $\delta B_d = 400 \mu\text{G}$. In the first row $z_0 = 10^{17} \text{ cm}$ and in the second $z_0 = 6 \times 10^{17} \text{ cm}$. The value of η_{crit} in each panel of Fig. 5 is then: 5.2 (upper left), 17 (upper center), 69 (upper right), 13 (lower left), 42 (lower center), and 170 (lower right). The downstream turbulence level $\delta B_d/B_d$ can be deduced at any given $|z|$ noting that it

is equal to $\delta B_d/(B_{d,0} \times (|z|/z_0)) = \eta_{\text{crit}}/(|z|/z_{\text{crit}})$. In every panel, all spectra are normalized to the same (arbitrary) level. The solid red line for the electrons injected at $|z|/z_0 \leq 0.02$ dominates over all other lines. A larger fraction of these particles is accelerated, than is the case for injection at larger $|z|$, and their spectrum is also harder. These results unambiguously confirm that electron acceleration to high energies preferentially happens for particles injected at small $|z|$, in line with the qualitative discussion in Sect. 3.1. As is visible in the lower right panel in Fig. 1, electrons injected at larger $|z|$ move towards the equatorial plane due to shock-drift, but most of them are advected into the downstream after a few cycles. Only a small fraction of them reaches the equatorial region, and this fraction decreases with the value of $|z|$ at injection. For instance, in the upper left panel in Fig. 5, the hard high-energy tail of the dashed orange spectrum for $0.02 < |z|/z_0 \leq 0.04$ ($3.46 < |z|/z_{\text{crit}} \leq 6.93$; $\eta_{\text{crit}} = 5.2$) is due to those few particles that have reached the equatorial region and are subsequently accelerated there. Indeed, this spectrum has about the same slope as the solid red one. The electrons that do not reach the equatorial region still gain some energy from their few shock crossings, and from shock-drift because the average change per cycle in $|z|$ is negative. This is the origin of the small energy gains experienced by particles injected at higher $|z|$, and of their ‘‘bump-like’’ spectra with low-energy cutoffs. See, for example, the spectra for $0.04 < |z|/z_0 \leq 0.06$ (dotted green lines), in the first column of Fig. 5, and those for $0.08 < |z|/z_0 \leq 0.10$ (solid magenta lines), in the second column.

For values of $|z|/z_0$ larger than those plotted in Fig. 5, the turbulence level $\delta B_d/B_d$ is so low that almost all injected electrons are advected away into the downstream and do not perform even a single cycle.

Comparing the three columns of Fig. 5, we also note that the width z_w of the favorable region where electrons

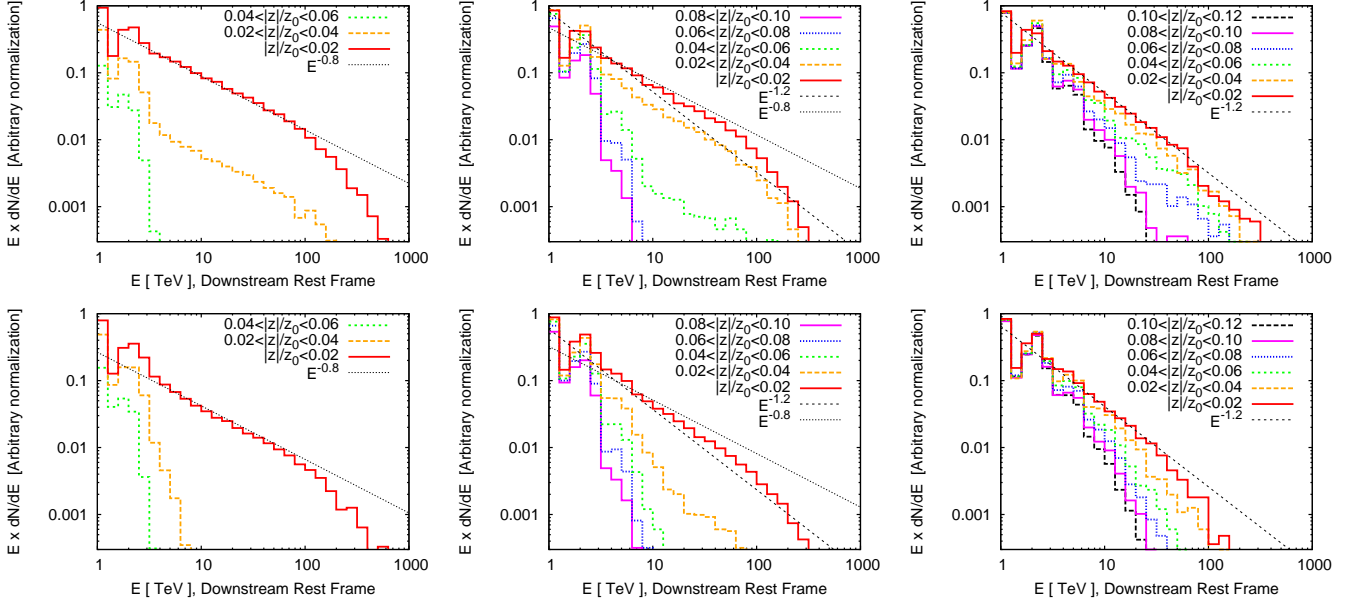


FIG. 5.— Electron spectra $E_d \times dN/dE_d$ in the DRF for injection close to the equatorial plane, $|z|/z_0 \leq 0.02$ (solid red lines), and in five zones of increasing altitude above it: $\zeta_i < |z|/z_0 < \zeta_{i+1}$, with $\zeta_i = 0.02 \times i$, $i = 1, \dots, 5$, corresponding to $\xi_i < |z|/z_{\text{crit}} < \xi_{i+1}$, with $\xi = (3.46, 6.93, 10.4, 13.9, 17.3, 20.8)$ in the first row, where $z_0 = 10^{17}$ cm, and with $\xi = (8.48, 17.0, 25.4, 33.9, 42.4, 50.9)$ in the second row, where $z_0 = 6 \times 10^{17}$ cm. In the first column $\delta B_d = 30 \mu\text{G}$, in the second $\delta B_d = 100 \mu\text{G}$, and in the third $\delta B_d = 400 \mu\text{G}$. The thin black dashed and dotted lines show power-laws $\propto E_d^{-1.2}$ and $\propto E_d^{-0.8}$, respectively.

can be accelerated to high energies grows with δB_d . This is unsurprising, because larger turbulence amplitudes in the downstream correspond to wider regions around the equatorial plane where the downstream turbulence levels $\delta B_d/B_d$ are sufficiently large for electrons to be scattered back into the upstream and be accelerated via the first-order Fermi mechanism. For instance, for $\delta B_d = 30 \mu\text{G}$ and $z_0 = 10^{17}$ cm (upper left panel), none of the electrons injected in the band $0.04 < |z|/z_0 \leq 0.06$ is accelerated to high energy. However, for $\delta B_d = 400 \mu\text{G}$ (upper right panel), acceleration in this band is almost as successful as for the central band with $|z|/z_0 \leq 0.02$. Indeed, the band $0.04 < |z|/z_0 \leq 0.06$ corresponds to a region with downstream turbulence levels of $0.5 < \delta B_d/B_d \leq 0.75$ in the upper left panel where $\eta_{\text{crit}} = 5.2$, and to $6.7 < \delta B_d/B_d \leq 10$ in the upper right one where $\eta_{\text{crit}} = 69$.

By comparing the two rows in Fig. 5, one can see that the relative width z_w/z_0 of the favorable region for electron acceleration decreases with z_0 at δB_d fixed. For example, for $z_0 = 10^{17}$ cm and $\delta B_d = 30 \mu\text{G}$ (upper left panel), acceleration to high energies still takes place in the band $0.02 < |z|/z_0 \leq 0.04$ (dashed orange line), whereas no acceleration to high energies is recorded in the same band for $z_0 = 6 \times 10^{17}$ cm (lower left panel), even though the downstream turbulence levels are the same in this band in both panels. Therefore, the width z_w of the favorable region for particle acceleration does not grow linearly with z_0 . It grows more slowly, roughly as z_{crit} and thence as $\sqrt{z_0}$ (i.e., $z_w/z_0 \propto 1/\sqrt{z_0}$). The band $0.02 < |z|/z_0 \leq 0.04$ corresponds to $3.46 < |z|/z_{\text{crit}} \leq 6.93$ in the upper left panel, and to $8.48 < |z|/z_{\text{crit}} \leq 17.0$ in the lower left panel. Indeed, the results for this band in the upper panel are similar to those in the band $|z|/z_0 \leq 0.02$ in the lower panel, which corresponds to $|z|/z_{\text{crit}} \leq 8.48$.

To expedite the simulations, we choose an upper

TABLE 2
FRACTION OF ACCELERATED ELECTRONS OVER THE WHOLE TS

$z_0/(10^{17} \text{ cm})$	$\delta B_d/(1 \mu\text{G})$	η_{crit}	$\epsilon_{\text{acc},7}$	\mathcal{F}_{inj}
1	0.6	0.10	3.19×10^{-4}	0.05
1	1	0.17	2.06×10^{-3}	0.05
1	3	0.52	6.99×10^{-3}	0.05
1	10	1.7	5.72×10^{-3}	0.05
1	30	5.2	1.01×10^{-2}	0.055
1	60	10	7.22×10^{-3}	0.08
1	100	17	5.78×10^{-3}	0.1
1	200	35	7.59×10^{-3}	0.1
1	300	52	6.42×10^{-3}	0.12
1	400	69	5.93×10^{-3}	0.17
6	0.6	0.25	3.24×10^{-4}	0.05
6	1	0.42	1.39×10^{-3}	0.05
6	3	1.3	3.47×10^{-3}	0.05
6	10	4.2	3.56×10^{-3}	0.05
6	30	13	4.15×10^{-3}	0.055
6	60	25	3.48×10^{-3}	0.08
6	100	42	3.33×10^{-3}	0.1
6	200	85	5.84×10^{-3}	0.1
6	300	1.3×10^2	5.26×10^{-3}	0.12
6	400	1.7×10^2	5.27×10^{-3}	0.17

NOTE. — Electrons are injected at $|z|/z_0 \leq \mathcal{F}_{\text{inj}}$ with energy 1 TeV. The regular field at z_0 is $B_{d,0} = 1 \text{ mG}$. $\epsilon_{\text{acc},7}$ is the fraction of injected particles accelerated to more than 7 TeV.

boundary on the relative size of the region where injected electrons can be accelerated to high energies: $|z|/z_0 \leq \mathcal{F}_{\text{inj}}$. A “generous” estimate is provided in the fifth column of Table 2, for δB_d within the range $(0.6 - 400) \mu\text{G}$, and for $z_0 = 10^{17}$ cm or $z_0 = 6 \times 10^{17}$ cm. We inject 10^6 electrons at the TS, in the region at $|z|/z_0 \leq \mathcal{F}_{\text{inj}}$. In the fourth column of Table 2, we provide the fraction $\epsilon_{\text{acc},7}$ of these electrons that are accelerated to energies $E_d \geq 7 \text{ TeV}$. We use here the condition $E_d \geq 7 \text{ TeV}$ because our simulations show that the overall electron spec-

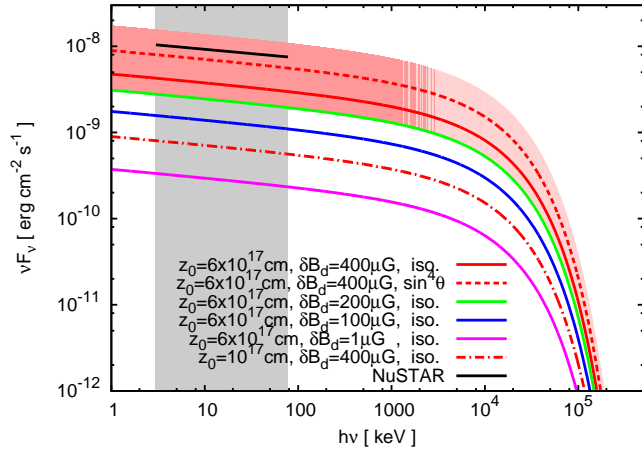


FIG. 6.— Predicted synchrotron spectra at $h\nu \geq 1$ keV for the Crab Nebula, versus NuSTAR measurements (Madsen et al. 2015, solid black line). Each line corresponds to a different combination of z_0 and δB_d , for isotropic (“iso.”) or $\propto \sin^4 \vartheta$ pulsar winds and for $D_{\text{Crab}} = 2.0$ kpc, see the key. Red area for the uncertainty on $\{z_0 = 6 \times 10^{17} \text{ cm}, \delta B_d = 400 \mu\text{G}\}$ for $1.5 \text{ kpc} \leq D_{\text{Crab}} \leq 2.5 \text{ kpc}$.

trum at the TS is well described by a power-law above this energy. We find that the spectrum below ≈ 7 TeV does not look like a perfect power-law, and displays a small bump due to the particles injected at large $|z|$. This can be seen qualitatively by summing up by eye the contributions from all bands in Fig. 5. These fractions $\epsilon_{\text{acc},7}$ depend on \mathcal{F}_{inj} , and multiplying them by $\mathcal{F}_{\text{inj}}/z_0$ gives the total acceleration efficiency for the whole TS in the striped wind region, in planar geometry. As already expected from Fig. 5, the total acceleration efficiency tends to grow with δB_d . The values for $\epsilon_{\text{acc},7}$ are smaller than those for $\epsilon_{\text{acc},3}$ in Table 1 because of the higher energy threshold (7 TeV), and because of the larger size of the studied region.

Finally, we note that positron acceleration, which is inefficient in the equatorial plane, shuts off completely at larger $|z|$.

3.4. Synchrotron X-rays from the Crab Nebula

Using the method described in Sect. 2.5, we compute the synchrotron spectrum, taking $B = 0.5$ mG for the strength of the magnetic field in which the electrons cool, and $E_{\text{max}} = 1$ PeV for their maximum energy at the TS, cf. Eq. (12). These values provide a high-energy cutoff in the synchrotron spectrum at roughly 30 MeV, which agrees with observations of the Crab Nebula, and lies well above the X-ray observations with which we compare our predictions. The cooling time of electrons of 1 PeV is roughly 10^6 s, corresponding to a region of size somewhat larger than the acceleration zone considered. The results of § 3.3 show the electron spectrum at the TS to be a power-law $\propto E^{\alpha_e}$ above $E_{\text{min}} = 7$ TeV (i.e., $f = 7$), which we can expect to extend up to E_{max} . The cooling time for electrons of E_{min} is roughly 10^8 s, corresponding to a size somewhat smaller than the X-ray nebula, and the energy of the photons emitted by these electrons is about 1 keV, which roughly defines the lower limit of the range we attempt to model.

Observations by NuSTAR (Madsen et al. 2015) give $\alpha_e \simeq -2.2$, which, from Fig. 4 (left panel) and Table 1 implies either $\delta B_d > 400 \mu\text{G}$ or $> 200 \mu\text{G}$ for

$z_0 = 10^{17}$ cm and 6×10^{17} cm, respectively. Or, alternatively, $\delta B_d < 1 \mu\text{G}$ or $\delta B_d < 0.4 \mu\text{G}$, again for $z_0 = 10^{17}$ cm and 6×10^{17} cm, respectively. (The case of harder spectra is discussed in Sect. 4.)

Assuming the Crab Nebula to be at a distance $D_{\text{Crab}} = 2.0$ kpc from Earth and that the particle flux from the pulsar is distributed in latitude in proportion to the wind power, with $n = 0$ or $n = 4$, we plot in Figure 6 the synchrotron spectra νF_ν at energies $h\nu \geq 1$ keV, for these values of z_0 and δB_d . The normalization is found using the values of $\epsilon_{\text{acc},7}$ and \mathcal{F}_{inj} from Table 2, assuming the equatorial radius of the TS is $r_{\text{TS}} = 4.3 \times 10^{17}$ cm, the spindown luminosity $L_{\text{s.d.}} = 5 \times 10^{38}$ erg s $^{-1}$ and the mass-loading parameter $\mu = 2 \times 10^6$. In this figure, the solid black line shows the approximate level of the NuSTAR data (Madsen et al. 2015) in the energy band $3 \text{ keV} \leq h\nu \leq 78 \text{ keV}$ (area shaded in grey). Our prescription of the electron spectrum below $E_d = 7$ TeV, given in Eq. (11), influences νF_ν for $h\nu \lesssim (2-3) \text{ keV}$. Since this is not relevant for NuSTAR data, we extrapolate the power-law in this figure to below 7 TeV.

The four solid lines in Figure 6 are calculated for an isotropic pulsar wind ($n = 0$) with $z_0 = 6 \times 10^{17}$ cm, which corresponds to $\Theta \simeq 80^\circ$, i.e. an almost orthogonal rotator. These four spectra are computed for $\delta B_d = 1 \mu\text{G}$ (magenta line), $\delta B_d = 100 \mu\text{G}$ (blue), $\delta B_d = 200 \mu\text{G}$ (green), and $\delta B_d = 400 \mu\text{G}$ (red). As expected, the level of the emission increases with δB_d . The line for $\delta B_d = 400 \mu\text{G}$ is still below NuSTAR data, but is compatible with it if one takes into account both the uncertainties on the distance to the Crab Nebula (± 0.5 kpc) and those on $L_{\text{s.d.}}$. In contrast, small values of Θ cannot explain the data. For instance, we show with the dashed-dotted red line, νF_ν for $z_0 = 10^{17}$ cm (i.e. $\Theta \simeq 13^\circ$) and $\delta B_d = 400 \mu\text{G}$: In this case, the predicted level of the emission is an order of magnitude below NuSTAR data. Finally, since the pulsar wind may be anisotropic, we plot, as an example, the case $n = 4$ (cf. Sect. 2.5) with $z_0 = 6 \times 10^{17}$ cm and $\delta B_d = 400 \mu\text{G}$ (dashed red line). The emission is enhanced by a factor ≈ 2 with respect to that for an isotropic wind with the same parameters, which raises it to the level of the NuSTAR data. We represent the uncertainty on the two lines with $\{z_0, \delta B_d\} = \{6 \times 10^{17} \text{ cm}, 400 \mu\text{G}\}$, caused by the estimate of the distance D_{Crab} to the Crab Nebula by the area shaded in red. This shows that the data are compatible with the above predictions, as well as with those for an anisotropic pulsar wind with a lower level of turbulence $\delta B_d = 200 \mu\text{G}$.

In our picture, electrons enter the Fermi acceleration process after thermalization at the TS to an injection energy $E_{\text{inj,d}} \sim \mu m_e c^2$. The computations reported in Fig. 6 are performed with $E_{\text{inj,d}} = 1$ TeV, which lies at the upper end of the permitted range. Repeating these for $E_{\text{inj,d}} = 10$ GeV leads to a reduction in the X-ray flux by a factor of approximately 25. This is due to reductions of the normalization of the electron spectrum in the radiating band, and of the size of the region around the equatorial plane where electron acceleration occurs, which are only partially compensated by the increased particle flux density compared to the total power density in the wind. Thus, in our model, such a low injection energy is incompatible with the X-ray observations of the Crab Nebula.

4. DISCUSSION AND PERSPECTIVES

The synchrotron spectrum of the Crab Nebula follows a power-law, $\nu F_\nu \propto \nu^{-0.1}$, in the X-ray band, according to observations by NuSTAR (Madsen et al. 2015). This corresponds to an accelerated electron spectrum at the TS with $\alpha_e \simeq -2.2$, close to the value -2.23 ± 0.01 predicted for the first-order Fermi mechanism operating at a parallel, ultra-relativistic shock in the presence of isotropic pitch-angle diffusion (Kirk et al. 2000). However, though ultra-relativistic, the termination shock of the wind of the Crab Pulsar is expected to be perpendicular, rather than parallel, which has led to suggestions that the Fermi process cannot provide an explanation of the X-ray spectrum (e.g., Olmi et al. 2016). The results presented in § 3 use an explicit model of the magnetic field at the termination shock to demonstrate that this mechanism is indeed viable. Physically, the reason is that the drift of particle orbits along the shock surface tends to focus either electrons or positrons (depending on the pulsar polarity) into the equatorial current sheet of the nebula. Here, the toroidal magnetic field is weak, and the level of turbulence suggested by global MHD simulations is sufficient to provide the scattering needed for the Fermi process to be effective.

In contrast to the case of a uniform magnetic field, we find that the spectral index for the more appropriate equatorial current sheet configuration depends on the amplitude of the turbulence. As can be seen in Fig. 4 (left panel), both weak and strong turbulence lead to $\alpha_e \simeq -2.2$, but there exists an intermediate range in which a harder spectrum with $\alpha_e \simeq -1.8$ is predicted. In this connection “weak” and “strong” refer to the turbulence level at that height in the sheet where the gyroradius of an injected particle equals its distance from the equatorial plane. I.e., in terms of the parameter defined in Eq. (5), $\eta_{\text{crit}} \ll 1$ and $\eta_{\text{crit}} \gg 1$. In the case of the Crab, only “strong” turbulence amplitudes and a relatively broad current sheet — as determined by the angle between the pulsar’s magnetic and rotation axes — are compatible with the flux level reported by NuSTAR. This conclusion rests on the assumption that the angular dependence of the particle flux carried by the wind is proportional to that of the total power. At first sight, it might seem that a scenario in which the particle flux is more strongly concentrated towards the equatorial plane would lead to an enhanced X-ray flux, and, therefore, relax the above constraints. However, an increase in the equatorial particle flux corresponds to a decrease in the effective value of μ , and, therefore, of the injection energy. As noted in § 3, this reduces the predicted X-ray flux. These remarks apply to the spatially integrated X-ray flux, and assume a level of turbulence that is constant in time. In principle, the level of turbulence close to the TS can fluctuate on the timescale of months. Our computations predict a harder synchrotron spectrum when $\eta_{\text{crit}} \sim 1 - 10$. Thus, the high spatial resolution observations by the Chandra X-ray Observatory (Mori et al. 2004), that reported a photon spectrum corresponding to $\alpha_e \simeq -(1.8 - 2.0)$ very close to the equator, may have sampled a lower turbulence level in this region of the Nebula.

In our model, particles are able to return to the shock because they propagate in a prescribed field of Gaussian

turbulence. This approach is motivated by MHD simulations of the global flow pattern, which show turbulence driven roughly on the scale of the radius of the TS, with an amplitude comparable to the ambient field strength outside the current sheet. It implicitly assumes that a turbulent cascade to smaller length scales develops, and fills the downstream region. We tested both Kolmogorov ($\mathcal{P}(k) \propto k^{-5/3}$) and Bohm ($\propto k^{-1}$) spectra, and did not find a significant impact on our results. This suggests that the choice of spectrum is not important, but we note that our limited dynamical range ($L_{\text{max}}/L_{\text{min}} \sim 100$) does not allow us to firmly rule out any dependence on $\mathcal{P}(k)$ in the case of $L_{\text{max}}/L_{\text{min}} \gg 100$.

On the other hand, in the upstream plasma, any turbulence present must either be imprinted at the launching point of the wind, or created by reflected particles and/or waves (Lemoine & Pelletier 2010; Casse et al. 2013). Since the amplitude of the former is difficult to estimate, and the latter effect is absent in our test-particle simulations, we performed a series of checks and verified that our results are unaffected by either the power-spectrum or the amplitude of the upstream turbulence, provided the latter does not greatly exceed $\sim 0.1 \mu\text{G}$. Complete neglect of the upstream turbulence, on the other hand, would introduce an unphysical artifact into our simulations, since a planar 1D treatment without upstream turbulence permits some particles on Speiser orbits to propagate to arbitrarily large distance upstream. In a more realistic picture, such orbits are eliminated by effects such as irregularities in the incoming wave and radiation losses of the particles, as well as the spherical geometry appropriate for a pulsar wind.

The main argument against Fermi acceleration as the mechanism responsible for producing the X-ray emitting electrons in the Crab Nebula is based on the results of PIC simulations (Sironi & Spitkovsky 2011), which show efficient acceleration at relativistic shocks only when the ambient field is approximately parallel to the shock normal and the magnetization parameter σ is small (typically $< 10^{-3}$). Because such conditions are expected on only a very small fraction ($\lesssim 1\%$) of the TS, through which a correspondingly small fraction of the wind power flows, particles accelerated there cannot carry the power needed to explain the observed X-ray emission (Amato 2014). However, currently available PIC simulations specify an initially uniform magnetic field, so that particles can return to the shock only by scattering on self-generated turbulence. In contrast, the scattering in our approach results from a turbulent field generated externally by the global flow pattern. The region of the TS in which particles are injected into the acceleration process reaches, in this case, a height of several times z_{crit} above the equator, corresponding to a few per cent of the area of the TS. The majority ($\gtrsim 90\%$) of the electrons carried by the wind do not enter the Fermi acceleration process. Although we do not address the fate of these electrons here, it is conceivable that another acceleration mechanism operates upon them, and may be responsible for the radio to optical emission of the Nebula (Olmi et al. 2016). It is important to note that during the course of Fermi acceleration, the area of the TS sampled by the particles grows in proportion to their energy. Therefore, although the number of participating particles is

restricted to those entering through a few per cent of the TS area, the available power is a much larger fraction of the wind luminosity, and is ultimately sufficient to produce the observed X-ray flux.

5. SUMMARY AND CONCLUSIONS

Using a global model of the magnetic field, we study the acceleration of electrons and positrons at the termination shock of a striped pulsar wind, and compute the resulting high-energy synchrotron emission. For parameters appropriate for the Crab Nebula, we find that either electrons or positrons — but not both — can be accelerated to \sim PeV energies via the first-order Fermi mechanism in a ring-shaped region of the TS, around the equatorial plane of the pulsar. The width of this ring grows with the downstream turbulence level. The Fermi mechanism shuts off outside this region because of the strong toroidal field at higher latitudes. Drifts along the surface of the TS focus the accelerating particles towards the equatorial plane, and maintain them on Speiser orbits around it. This favors acceleration via the first-order Fermi mechanism, because it causes them to cross the TS and re-enter downstream near this plane, where the toroidal field is weakest and the turbulence level is largest. In contrast, drifts along the shock push particles of the disfavored charge away from this region, thus hampering their acceleration. The sign of charge that is accelerated depends on the pulsar polarity. In-

terestingly, modeling of the multi-wavelength emission of the Crab Nebula suggests that the particles responsible for X-ray emission are indeed accelerated close to the equatorial plane (Olmi et al. 2016).

The predicted spectral index of the accelerated particles is in the range $\alpha_e \simeq -1.8$ to -2.4 , and depends on the downstream turbulence level, being primarily determined by the electron return probability from the downstream to the upstream, cf. Fig. 4. For turbulence levels $\eta_{\text{crit}} \ll 1$ or $\gg 10$ — cf. Eqs. (5) and (4) — we find that $\alpha_e \simeq -2.2$, which is consistent with the photon index $\Gamma = 2.1$ measured for the Crab Nebula in 1 – 100 keV X-rays (Madsen et al. 2015). The observed X-ray flux can be reproduced for $\eta_{\text{crit}} \gg 10$, provided the angle between the magnetic and rotation axes of the pulsar is sufficiently large, cf. Fig. 6. The electron spectrum hardens to $\alpha_e \simeq -1.8$ to -2.0 when $\eta_{\text{crit}} \approx 1 - 10$, which may explain the hard photon index $\Gamma \simeq 1.9$ to 2.0 observed by the Chandra X-ray Observatory in the central regions of the Crab Nebula (Mori et al. 2004). Taking account of the dependence of the spectral index on the level of turbulence (η_{crit}) may also offer an explanation of the X-ray emission of other pulsar-wind nebulae.

We thank Uri Keshet for useful discussions. This research was supported by a Grant from the GIF, the German-Israeli Foundation for Scientific Research and Development.

REFERENCES

- Achterberg, A., Gallant, Y. A., Kirk, J. G., & Guthmann, A. W. 2001, *MNRAS*, 328, 393, astro-ph/0107530
 Amano, T., & Kirk, J. G. 2013, *ApJ*, 770, 18, 1303.2702
 Amato, E. 2014, in *International Journal of Modern Physics Conference Series*, Vol. 28, International Journal of Modern Physics Conference Series, 1460160, 1312.5945
 Bednarz, J., & Ostrowski, M. 1998, *Physical Review Letters*, 80, 3911, astro-ph/9806181
 Begelman, M. C., & Kirk, J. G. 1990, *ApJ*, 353, 66
 Bell, A. R. 1978, *MNRAS*, 182, 147
 Casse, F., Marcowith, A., & Keppens, R. 2013, *MNRAS*, 433, 940, 1305.0847
 Coroniti, F. V. 1990, *ApJ*, 349, 538
 Del Zanna, L., Pili, A. G., Olmi, B., Bucciantini, N., & Amato, E. 2018, *Plasma Physics and Controlled Fusion*, 60, 014027, 1711.01120
 Giacchè, S., & Kirk, J. G. 2017, *ApJ*, 835, 235, 1612.04282
 Giacinti, G., Kachelrieß, M., Semikoz, D. V., & Sigl, G. 2012, *JCAP*, 7, 031, 1112.5599
 Kirk, J. G., & Giacinti, G. 2017, *Physical Review Letters*, 119, 211101, 1710.04493
 Kirk, J. G., Guthmann, A. W., Gallant, Y. A., & Achterberg, A. 2000, *ApJ*, 542, 235, astro-ph/0005222
 Kirk, J. G., & Schneider, P. 1987, *ApJ*, 315, 425
 Kirsch, M. G. et al. 2005, in *Proc. SPIE*, Vol. 5898, UV, X-Ray, and Gamma-Ray Space Instrumentation for Astronomy XIV, ed. O. H. W. Siegmund, 22–33, astro-ph/0508235
 Lemoine, M., & Pelletier, G. 2010, *MNRAS*, 402, 321, 0904.2657
 Lyubarsky, Y. E. 2003, *MNRAS*, 345, 153, astro-ph/0306435
 Madsen, K. K. et al. 2015, *ApJ*, 801, 66, 1502.07765
 Melrose, D. B. 1980, *Plasma astrophysics. Nonthermal processes in diffuse magnetized plasmas - Vol.1: The emission, absorption and transfer of waves in plasmas; Vol.2: Astrophysical applications*
 Michel, F. C. 1994, *ApJ*, 431, 397
 Mori, K., Burrows, D. N., Hester, J. J., Pavlov, G. G., Shibata, S., & Tsunemi, H. 2004, *ApJ*, 609, 186, astro-ph/0403287
 Olmi, B., Del Zanna, L., Amato, E., & Bucciantini, N. 2015, *MNRAS*, 449, 3149, 1502.06394
 Olmi, B., Del Zanna, L., Amato, E., Bucciantini, N., & Mignone, A. 2016, *Journal of Plasma Physics*, 82, 635820601, 1610.07956
 Porth, O., Buehler, R., Olmi, B., Komissarov, S., Lamberts, A., Amato, E., Yuan, Y., & Rudy, A. 2017, *Space Sci. Rev.*, 207, 137, 1703.05184
 Porth, O., Komissarov, S. S., & Keppens, R. 2014, *MNRAS*, 438, 278, 1310.2531
 Porth, O., Vorster, M. J., Lyutikov, M., & Engelbrecht, N. E. 2016, *MNRAS*, 460, 4135, 1604.03352
 Sironi, L., & Spitkovsky, A. 2011, *ApJ*, 741, 39, 1107.0977
 Speiser, T. W. 1965, *J. Geophys. Res.*, 70, 4219
 Summnerlin, E. J., & Baring, M. G. 2012, *ApJ*, 745, 63, 1110.5968
 Tchekhovskoy, A., Philippov, A., & Spitkovsky, A. 2016, *MNRAS*, 457, 3384, 1503.01467